Journal of Materials Science: Materials in Electronics (2019) 30:11508–11519
https://doi.org/10.1007/s10854-019-01506-7

Fast and continuous obtaining of Eu^{3+} doped CeO_2 microspheres by ultrasonic spray pyrolysis: characterization and photocatalytic activity

A. A. G. Santiago[1] · N. F. Andrade Neto[1] · E. Longo[2] · C. A. Paskocimas[1] · F. V. Motta[1] · M. R. D. Bomio[1]

Received: 9 March 2019 / Accepted: 13 May 2019 / Published online: 17 May 2019

Abstract
In this work, CeO_2:xEu^{3+} ($x = 0$, 0.01, 0.02, 0.04 and 0.08 mol%) microspheres were obtained by the fast and continuous ultrasonic spray pyrolysis method. Powders were characterized by X-ray diffraction (XRD), X-ray fluorescence analysis (XRF), scanning electronic microscopy (FESEM), Raman spectra, UV–Visible spectroscopy (UV–Vis) and photocatalytic activity. All XRD patterns were indexed by the cubic structure of the fluorite type, without the presence of secondary phases, indicating success in the Eu^{3+} doping in the CeO_2 structure. In addition, The XRF analysis confirmed the presence of Eu in the CeO_2 powders. In the Raman spectra of the samples occurs the vibrational mode F_{2g}, which is a characteristic band of materials with the fluorite type structure. Moreover, as the Eu^{3+} ion increased, it was noticed the appearance of additional bands referring to oxygen vacancies. FESEM showed that the CeO_2:xEu^{3+} particles have a spherical morphology with homogeneous chemical composition and particle size between 73 and 1560 nm. It can be seen a slight increase of defects in their morphology as the Eu^{3+} ion increases. The band gap varies between 3.22 and 3.28 eV, being influenced by defects in oxygen vacancies and the concentration of Ce^{3+} ion. The addition of Eu^{3+} generates the introduction of intermediary levels in the conduction band of CeO_2, besides increasing the reactive species effects, favoring the photocatalysis of Rhodamine B dye.

1 Introduction

A large consumption of water, energy and chemicals by industries, especially the textile industry, has been damaging the environment due to the release of toxic in effluents [1]. It is necessary to carry out some treatment in the residual waters of the textile processes because they usually present wealth color, inorganic salts, chemical oxygen demand (COD), pH and salinity, for example [2]. Synthetic origin dyes containing aromatic rings and azo groups are the most commonly used ones [3], with azo dyes being used by 60–70% of the dye market [4]. The photocatalytic reaction is the most efficient one in dye removal from effluents compared to other methods, by its operation in smooth conditions, strong oxidation capacity and reuse of the catalysts [5]. The development of semiconductor materials with photocatalytic activity has been object of study in several researches, trying to obtain materials with higher catalytic activities [6–11].

Cerium oxide (CeO_2) has been recurrently studied because of its corrosion stability, physical and chemical properties, chemical and biological strength. It is used as an heterogeneous catalyst for the degradation of organic pollutants and dyes due to its rapid change from Ce^{3+} to Ce^{4+} states, capacity of oxygen storage, its reuse and absorption only of UV light [12–14].

CeO_2 has a cubic structure of the fluorite type with space group *Fm-3m*, formed by one Ce^{4+} cation coordinated by eight O^{2-} anions [15]. In the literature, it is reported several promising applications for CeO_2 as a catalyst to reform vapor of propylene glycol in microreactors [16], gas sensor [17], opto-magnetic [18], catalysis of NO reduction [19], CO oxidation [20], electrolyte for solid oxide fuel cells [21, 22], antibacterial agent [23, 24] and phosphors [25–27], for example. Different routes of synthesis are used for CeO_2 to

Electronic supplementary material The online version of this article (https://doi.org/10.1007/s10854-019-01506-7) contains supplementary material, which is available to authorized users.

✉ A. A. G. Santiago
andersonsantiago@ufrn.edu.br

[1] LSQM, DEMAT, UFRN, Av. Sen. Salgado Filho, 3000, Natal, RN CEP 59072-970, Brazil

[2] CDMF-UFSCar, Universidade Federal de São Carlos, P.O. Box 676, São Carlos, SP 13565-905, Brazil

achieve these interesting properties and applications such as solid state reaction [28, 29], sol–gel [30], coprecipitation [31], conventional hydrothermal [32], microwave-assisted hydrothermal [33, 34], sonochemistry [35] and ball milling [36].

Recently, several materials have been synthesized by the ultrasonic spray pyrolysis (USP) method [37–44]. This method consists of atomizing or nebulizing a precursor solution by a device of ultrasonic frequencies, forming droplets that will experiment physicochemical phenomena, resulting in the evaporation of the solvent, precipitation and drying of the solutes to create fine powders with a spherical morphology [45, 46]. Some studies describe the synthesis of CeO_2 particles by the USP method, with or without doping gadolinium (Gd) or samarium (Sm) [47–52]. Jung et al. [53] synthesized CeO_2:Eu^{3+}/M^+ (M = Li, Na, and K) nanoparticles using the USP method and successive calcination at 1100 °C for 3 h and studied its luminescent properties. Min et al. [54] obtained CeO_2:Eu^{3+}/Na^+ nanoparticles via USP and successive calcination with temperature varying from 900 to 1100 °C for 3 h and studying the photoluminescent properties. However, the photocatalytic properties of CeO_2:Eu^{3+} synthesized by the USP method have not been explored.

In this work, the CeO_2:xEu^{3+} powders (x = 0, 0.01, 0.02, 0.04 and 0.08 mol%) were obtained in a single step by the USP method. The time for the particle to be formed inside the reactor was approximately 1 min. The correlation of the photocatalytic activity with doped Eu^{3+} ions are replaced be the Ce^{4+} ions in the CeO_2 crystal structure which was investigated.

2 Experimental

2.1 Preparation of CeO_2:xEu^{3+} powders

CeO_2:xEu^{3+} (x = 0, 0.01, 0.02, 0.04 and 0.08 mol%) powders were prepared using the ultrasonic spray pyrolysis method [55, 56]. Cerium nitrate ($Ce(NO_3)_3$, Aldrich), europium nitrate ($Eu(NO_3)_3$, Alfa Aesar) and distilled water were used to prepared the CeO_2:xEu^{3+} powders. The precursor solution, to x = 0, was prepared dissolving 3.75 mmol of cerium nitrate in 150 mL of distilled water and the other precursors solutions (x = 0.01, 0.02, 0.04 and 0.08 mol%) were realized according to stoichiometry. The ultrasonic spray pyrolysis equipment (Fig. S1) composed: nebulizer with 2.4 MHz of frequency; reactor (quartz tube with 50 mm diameter and 1.1 m of length); tubular horizontal electric furnace of the double heat zone (600 °C for zone 1 and 800 °C for zone 2); air flow (at 3 L min^{-1}); and, electrostatic precipitation (of stainless-steel tube). The precursor solution was atomized using the nebulizer, then the sprayed droplets were transported by means of the reactor, heated by the tubular electric furnace and transformed into solids particles inside the reactor. At last, the resultant particles were collected by means of electrostatic precipitation in the reactor exit. Estimated time of formation of the particles is about 1 min.

2.2 Characterization of CeO_2:xEu^{3+} powders

CeO_2:Eu^{3+} powders were characterized by XRD 7000, 40 kV and 30 mAh XRD (Shimadzu, model XRD 7000) with CuKα radiation (λ = 1.5406 Å), 2θ from 10° to 80° with the step speed of 1° min^{-1}. While for the Rietveld refinement measurement, it was utilized 2θ range from 10° to 120° with step size of 0.02° min^{-1}. Elemental X-ray fluorescence analysis (XRF) was performed on the Shimadzu EDX-720 spectrometer to analyze the Eu^{3+} doping efficiency in CeO_2. Raman spectrum was been obtained using Micro Raman Chromex 2000 using 532 nm line of frequency doubled Nd:YAG laser with range of 200 and 1200 cm^{-1}. Field-emission gun scanning electron microscopy and EDS spectroscopy (FESEM; Carl Zeiss, Supra 35-VP Model, Germany, operated at 6 kV or 14 kV) were using for investigated of the morphologies and dispersion of atoms of samples. Shimadzu spectrophotometer (UV-2600 model) was utilized for measurement of UV–Vis reflectance spectra of the powders.

The photocatalytic properties of the samples were tested (as a catalyst agent) for the degradation of Rhodamine B (RhB) dye with a molecular formula [$C_{28}H_{31}ClN_2O_3$] (99.5% purity, Mallinckrodt) in an aqueous solution under UV-light illumination. The sample was placed in a cylindrical quartz reactor, containing 50 mL of Rhodamine B dye solution (concentration 1×10^{-5} mol L^{-1}). Then, a cylindrical quartz reactor was placed into a photo-reactor at controlled temperature (25 °C) and, illuminated by six UVC lamps (TUV Philips, 15 W, with maximum intensity of 254 nm = 4.9 eV). In 20-min intervals, the 3 mL aliquot of the dye solution was taken and analyzed by its variations of the maximum absorption band of RhB dye solutions by UV–Vis absorbance spectra measurements using a Shimadzu spectrophotometer (UV-2600 model). The evaluation of the mechanism acting on the photocatalysis of Rhodamine B occurred by the use of radical inhibitors. For this, EDTA, isopropyl alcohol and $AgNO_3$ were used for the suppression of h^+,.OH and e^-, respectively.

3 Results and discussion

3.1 X-ray diffraction (XRD) and X-ray fluorescence (XRF)

Figure 1 shows that the XRD patterns for CeO_2 samples doped with Eu^{3+}. The XRD patterns were indexed in a unit cell in a fluorite cubic crystal structure *Fm-3m* (225) and

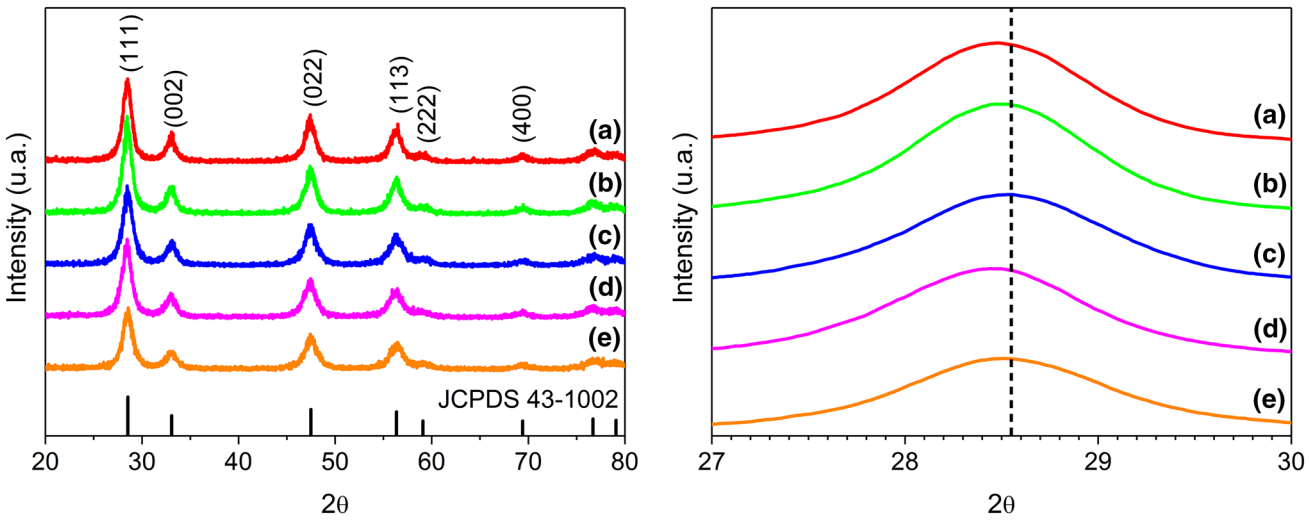

Fig. 1 XRD patterns to (a) CeO_2, (b) CeO_2:0.01Eu^{3+}, (c) CeO_2:0.02Eu^{3+}, (d) CeO_2:0.04Eu^{3+} and (e) CeO_2:0.08Eu^{3+}

lattice parameter a = 5.4113 Å, according to the JCPDS 43-1002 datasheet. The peaks show good intensity, showing that they are samples with a long-range crystalline structure. No additional peaks were identified, showing that there were pure phase standards and that doping occurred satisfactorily.

To confirm the substitution of Ce ions by Eu, X-ray fluorescence analysis (XRF) was performed. Figure S2 shows the spectra obtained for samples doped with 1, 2, 4 and 8% cerium. All measurements were performed under vacuum atmosphere. According to Fig. S1, there is the formation of the peaks corresponding to the characteristic transitions Lα, Lλ, $L\beta_1$, $L\beta_2$, $L\gamma_1$ and $L\gamma_2$ in 4.29, 4.84, 5.26, 5.61, 6.05 and 6.48 keV for Ce^{4+}. As the amount of Eu^{3+} is increased, the intensity of the peaks corresponding to the transitions Lα, $L\beta_2$ and Lγ in 5.84, 6.84 and 7.48 keV referring to the Eu^{3+} transitions is also increased. The results are in agreement with those reported in the literature [57, 58].

The Rietveld refinement method [59] was employed in order to explain possible differences in the structural arrangements induced by the Eu^{3+} doping in CeO_2. The General Structure Analysis System (GSAS) with the EXPGUI graphical interface [60] was used to perform this refinement. The datasheet used in the refinement was the ICSD 28753. The parameters used in the refined ones were: scaling factor and phase fraction; background (Chebyshev polynomial function); peak shape (Thomson-Cox-Hastingp-seudo-Voigt); changes in the network constants; fractional atomic coordinates; and isotropic thermal parameters. Figure 2 and Table 1 shown the results obtained for the Rietveld refinement.

The sample patterns are well matched to the ICSD 28753. Note that the Obs-Calc line exhibit the near rectilinear shape. Thus, differences between the experimentally observed XRD patterns and the theoretically calculated data are close to zero. Reliability parameters χ^2, R_{wp} and R_p show low values, indicating good quality of structural refinement and numerical results. These data confirm that the samples are isostructural, being the crystals well adapted to the cubic fluorite structure with the spatial group *Fm-3m* (225).

It can be seen that the lattice parameters (a) and, consequently, the unit cell volume of the samples increases together as Eu^{3+} doping increases (Table 1). This occurs due to the cationic substitution of Ce^{4+} by Eu^{3+} to promote a slight expansion of the unit cell, because the cations of Eu^{3+} have higher ionic radii than the cations of Ce^{4+}, which have an ionic radius of 1.066 Å and 0.970 Å, respectively [61]. The values obtained from the occupation of the Ce^{4+} and Eu^{3+} cations in the unit cell, are close to the synthesis stoichiometric, confirming that the doping was successfully performed.

The positions *x*, *y* and *z* occupied by the atoms in the unit cell did not change, maintaining the position of the Ce^{4+}/Eu^{3+} cations being $x = y = z = 0.00$ and the O^{2-} anions being $x = y = z = 0.25$. The fluorite cubic crystal structure of CeO_2 is formed by the Ce^{4+}/Eu^{3+} cations arranged in the face-centered cube surrounded by eight O^{2-} anions, while the O^{2-} anions are arranged in the tetrahedral positions linked to four Ce^{4+}/Eu^{3+}cations. Figure 3 shows the unit cells of the samples, obtained from the Rietveld refinement data.

3.2 Raman spectroscopy

Figure 4 shows the Raman spectra of the CeO_2:xEu^{3+} samples obtained by the USP method. The Raman spectroscopy was used to identify possible structural changes of order and disorder. The first order Raman phonon spectrum for a perfect crystal is formed by narrow lines, which correspond to the center point modes of the Raman allowed zones, which

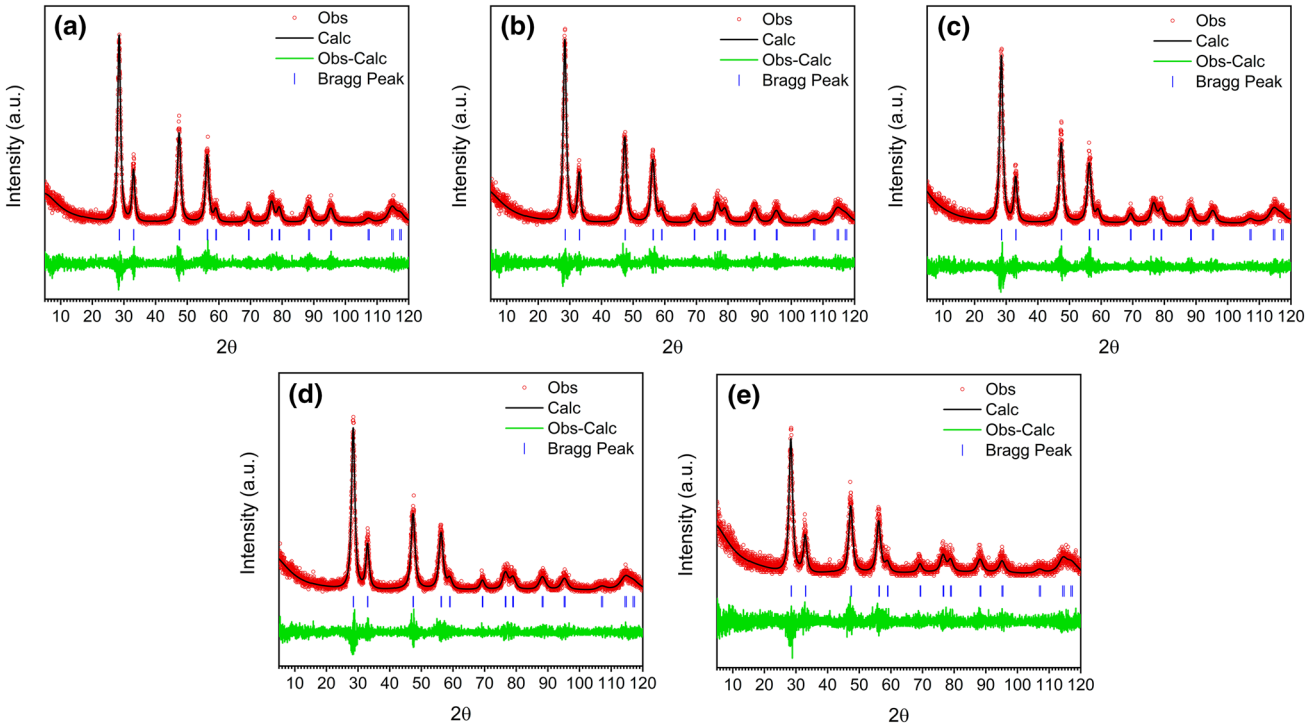

Fig. 2 Rietveld refinement of **a** CeO_2, **b** CeO_2:0.01Eu^{3+}, **c** CeO_2:0.02Eu^{3+}, **d** CeO_2:0.04Eu^{3+} and **e** CeO_2:0.08Eu^{3+}

Table 1 Rietveld refined structural parameters for the CeO_2:Eu^{3+}

Sample	CeO_2	CeO_2:0.01Eu^{3+}	CeO_2:0.02Eu^{3+}	CeO_2:0.04Eu^{3+}	CeO_2:0.08Eu^{3+}
a (Å)	5.414	5.418	5.418	5.422	5.423
Cell volume (Å^3)	158.7	159.0	159.1	159.4	159.5
Crystallite size (nm)	6.50	5.57	5.51	5.19	5.51
Microstrain ($\times 10^3$)	3.44	4.07	4.08	4.37	3.99
χ^2	1.286	1.259	1.249	1.275	1.302
R_{wp}	0.2306	0.2272	0.2298	0.2321	0.2675
R_p	0.1662	0.1602	0.1655	0.1668	0.1981
Occ					
Ce^{4+}	1.00	0.98	0.97	0.95	0.91
Eu^{3+}	0.00	0.01	0.02	0.04	0.08

follow the defined rules of polarization [62]. While for cluttered crystals, it is expected features such as the amplification of Raman rows of first order, activation of Raman forbidden phonons, appearance of large Raman bands reflecting the phonon density of states, frequency shifts of some peaks proportional to the concentration of the dopant element and division of some peaks involving distinct elements that carry the same site of the network [62].

The CeO_2 has a fluorite structure, of the *Fm-3m* (O_h^5) spacial group, so its vibrational structure is exceptionally simple with an active IR phonon of symmetry T_{1u} and active Raman phonon of symmetry F_{2g} at $k=0$. The first order of the CeO_2 Raman spectrum is characterized by the presence of a F_{2g} vibrational mode around 465 cm^{-1} for a single crystal, ascribed to the symmetric breathing mode of the oxygen atoms together at the Ce^{4+} cation [63].

In Fig. 4a it is seen the Raman spectrum of the CeO_2 sample without doping. Note the presence of two bands around 455 and 1050 cm^{-1}. The band at 455 cm^{-1} corresponds to the vibrational mode F_{2g}, described above. The vibrational mode F_{2g} is associated with the elongation of the Ce–O bond, where Ce and O are coordinated at eight and four times, respectively [64]. Thus, small changes in the bonds between Ce–O will promote the displacement of the band position, so there is a difference between the band position of a CeO_2 (465 cm^{-1}) single crystal and the CeO_2 sample

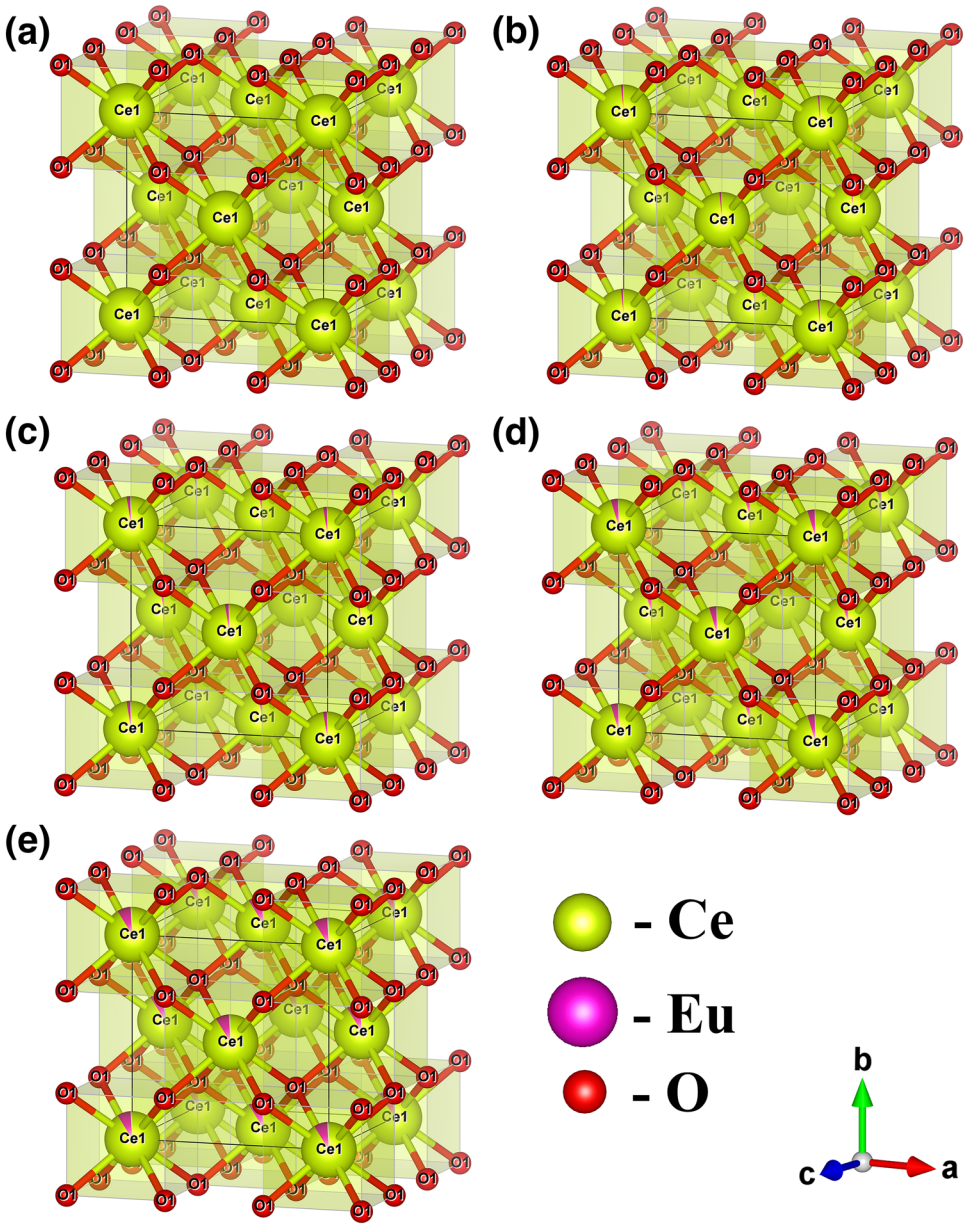

Fig. 3 Model of fluorite cubic structure of the **a** CeO_2, **b** CeO_2:0.01Eu^{3+}, **c** CeO_2:0.02Eu^{3+}, **d** CeO_2:0.04Eu^{3+} and **e** CeO_2:0.08Eu^{3+}

synthesized by the USP method (455 cm^{-1}). The weak band observed at 1050 cm^{-1} may be related to the asymmetry of the primary A_{1g}, combined with small additional contributions of symmetries of E_g and F_{2g} [63].

In the CeO_2 samples doped with Eu^{3+}, additional bands around 534 cm^{-1} and 600 cm^{-1} appear in the Raman spectra, as can be seen in Fig. 4. These additional bands are related to oxygen defects in the CeO_2 structure due to the difference in the atomic radius and the valence state of the dopant material in relation to the host material [65].

Oxygen vacancies are produced to compensate the negative charge generated by the replacement of the Ce^{4+} cations by the of Eu^{3+} cations, being more intense with the increase in the dopant amount. Defects produce new broad features higher energy (535–835 cm^{-1}) due to the contribution of acoustic and optical non-center Brillouin zone modes [66]. It was not observed the presence of the phonon mode which is a characteristic of the cubic phase of Eu_2O_3, characterized by the intense band near 340 cm^{-1} [67]. Thus, the presence of the characteristic bands of oxygen defects in the CeO_2 structure and the absence of the characteristic band of the Eu_2O_3 phonon reinforce that the Eu^{3+} cations are replacing the Ce^{4+} cations in the CeO_2 lattice.

The presence of a small band in the non-doped CeO_2 sample in 600 cm^{-1} can be noted. This band may be related to the crystallite size difference and the presence of Ce^{3+} cations on the surface of the solid promoting a non-stoichiometric condition and the appearance of this band in 600 cm^{-1} [63].

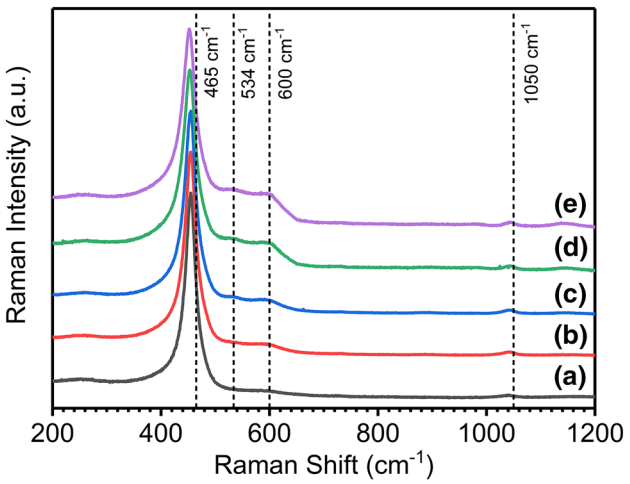

Fig. 4 Raman spectra of (a) CeO_2, (b) CeO_2:0.01Eu^{3+}, (c) CeO_2:0.02Eu^{3+}, (d) CeO_2:0.04Eu^{3+} and (e) CeO_2:0.08Eu^{3+}

3.3 Scanning electronic microscope (FESEM)

Figure 5 shows the FESEM micrographs of CeO_2:xEu^{3+} (x = 0.01, 0.02, 0.04 and 0.08 mol%) samples. The morphology of the particles is microspheres formed by nanoparticles, predominantly, with a diameter ranging from 73 to 1560 nm. It can be observed that the microspheres of the non-doped CeO_2 (Fig. 5a), have a surface with a number of defects, such as holes and irregularities, with lower intensity, being observed on the surface of CeO_2:0.08Eu^{3+} microspheres a higher amount of these defects (Fig. 5i). Messing et al. [68] report that various physical phenomena occur during the Spray Pyrolysis process, such as evaporation of the solvent on the surface of the droplet and diffusion of solvent vapors away from the drop in the gas phase, for example. Moreover, they show that particles from metal nitrates, most often form porous or irregular particles because the metallic nitrates melt before the solvent is completely removed, causing the inhibition of the solvent removal by the formed molten salt [68].

Min et al. [54] and Jung et al. [53] obtained CeO_2:Eu^{3+} particles by the spray pyrolysis method with subsequent calcination and obtained spherical-like and hollow-like particles. Shih et al. [52] reported that they observed CeO_2 particles produced by the spray pyrolysis method using cerium nitrate with a spherical solid form, porous spherical and porous concave, It was presented as its main reason the 60 °C melting temperature of cerium nitrate which inhibited the removal of the water entrapped in the porous spherical particles and that even larger particles can receive large deformation forces to induce fracture by breaking the porous structures into hollow concave particles.

Cerium nitrate exhibits solubility of 176 g/100 g H_2O at 25 °C and melting temperature of 150 °C, while europium nitrate exhibits solubility of 193 g/100 g H_2O at 25 °C and melting temperature at 85 °C [69]. It is believed that the stoichiometric increase of europium nitrate in the precursor solution promotes a greater inhibition of the water removal by the cerium/europium compound molten salt because of the low melting point of the europium nitrate, promoting an

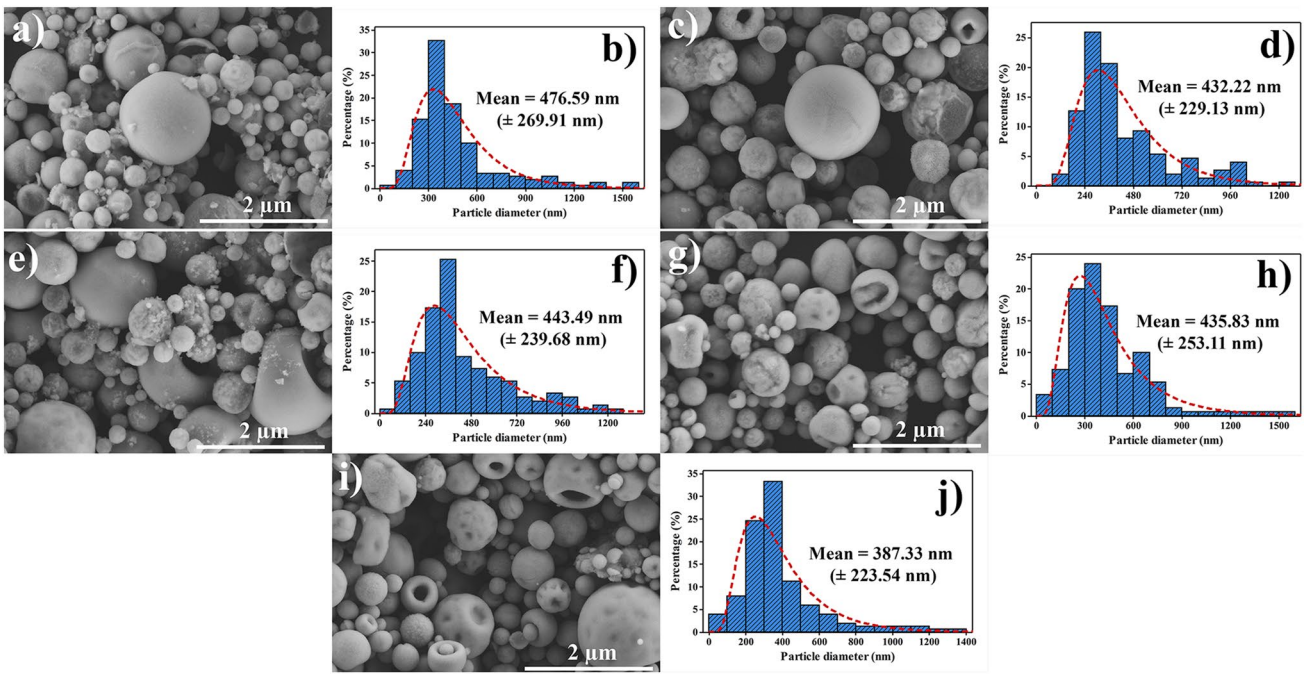

Fig. 5 FESEM micrographs of **a** CeO_2, **b** CeO_2:0.01Eu^{3+}, **c** CeO_2:0.02Eu^{3+}, **d** CeO_2:0.04Eu^{3+} and **e** CeO_2:0.08Eu^{3+}

increase of porous spherical particles and irregular porous. As the metal nitrates used in the precursor solution of CeO_2:xEu^{3+} have a high supersaturation in water, they tend to form a high number of crystallites of nanometric sizes [68], which form the microspheres.

Figure 6 shows the EDS spectrum and the mapping of the atomic distribution of CeO_2:$0.08Eu^{3+}$ sample. The EDS spectrum confirms the existence of the Eu atoms in the CeO_2 particles and together with the mapping reveals the compositional homogeneity of the Eu atoms in the particles.

3.4 UV–Vis reflectance

It was used the diffuse reflectance spectroscopy in the visible ultraviolet region to estimate the band gap of the CeO_2:Eu^{3+} powders. The Kubelka–Munk function [70] was used to estimate the value of the optical band gap (E_{gap}). In the Wood and Tauc method, the band gap is given by $F(R)hv \propto (hv - E_{gap})^k$, where h is the Planck constant, v is the frequency, $F(R)$ is the absorbance and k is indicated for the different transitions. For the CeO_2:Eu^{3+} powders, it was admitted $k = 1/2$, i.e., permissible direct, indicating a permissible direct electronic transition. Absorbance versus photon energy (eV) graphs was plotted and the linear portion of the curve was extrapolated for zero absorption to estimate E_{gap}.

Figure 7 and Table 2 present the estimated values for the band gap of the CeO_2:xEu^{3+} samples ($x = 0.01$, 0.02, 0.04 and 0.08 mol%) together with the values found in the literature. It can be seen that the non-doped CeO_2 sample presents the lowest band gap, followed by the increase of the band gap in the samples with doping values of 1 and 2 mol% Eu^{3+} and with a subsequent reduction of the band gap in the samples with doping values of 4 and 8% of mol of Eu^{3+}.

The band gap of CeO_2 is related to the creation of oxygen vacancies in the cerium oxide lattice, which allows the formation of energy states located between the O 2p (valence band) and Ce 4f states [73]. The concentration of Ce^{3+} specimens also influences the CeO_2 band gap, because the elevation of these specimens concentration displace to the red one the UV absorption profile, causing a decrease in the band gap [74]. The Ce^{3+} specimens may be located at the grain boundaries and also be related to the morphology of the samples, which influence the ratio from Ce^{3+} to Ce^{4+}, resulting in defects associated with Ce^{3+} ions and oxygen vacancies and red shift in the Ce^{3+} band gap [75].

Thus, we assume that the CeO_2:$0.01Eu^{3+}$ and CeO_2:$0.02Eu^{3+}$ samples present higher bands gap because of their low concentration of oxygen vacancies generated by Eu^{3+} doping, and a possible low concentration of Ce^{3+} as seen in Raman. While the CeO_2:$0.04Eu^{3+}$ and CeO_2:$0.08Eu^{3+}$ samples, exhibit a lower band gap due to a higher concentration of vacancies generated by Eu^{3+} doping and a benefit from the increasing concentration of Ce^{3+} specimens. In other words, the generation of oxygen vacancies and Ce^{3+} specimens occur simultaneously because of the charge compensation mechanism [76, 77]. Thus, the higher the doping of Eu^{3+} cations, the greater the generation of oxygen vacancies (Fig. 4) and, a higher occurrence of Ce^{3+} specimens will occur as a consequence for the charge compensation.

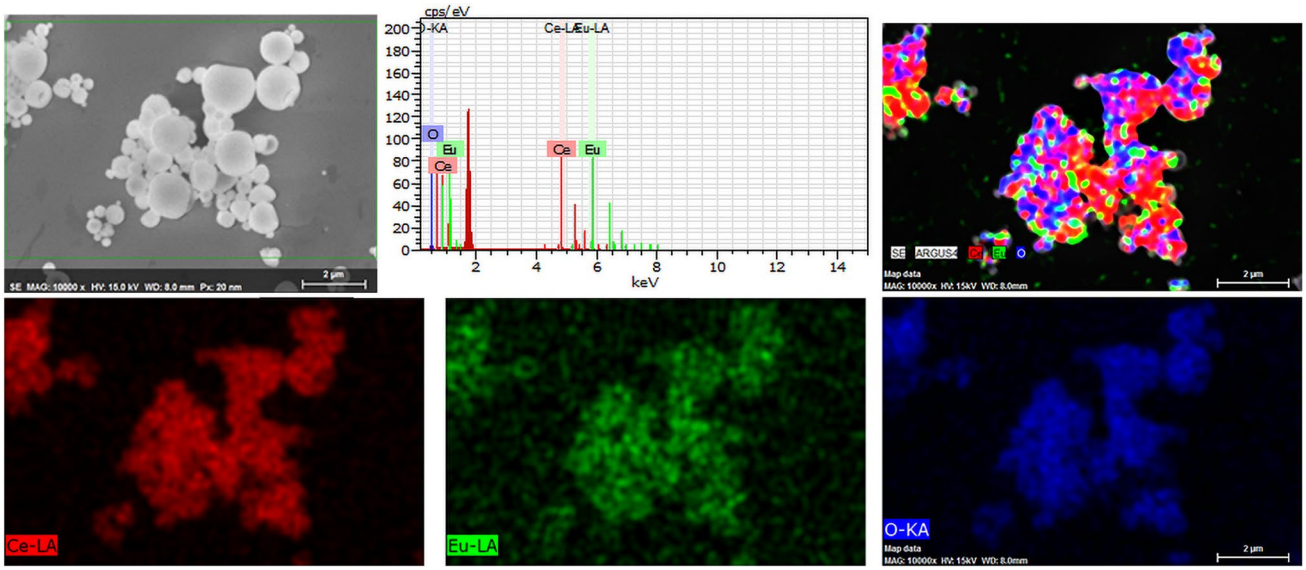

Fig. 6 EDS spectrum and mapping of atoms of CeO_2:$0.08Eu^{3+}$ sample

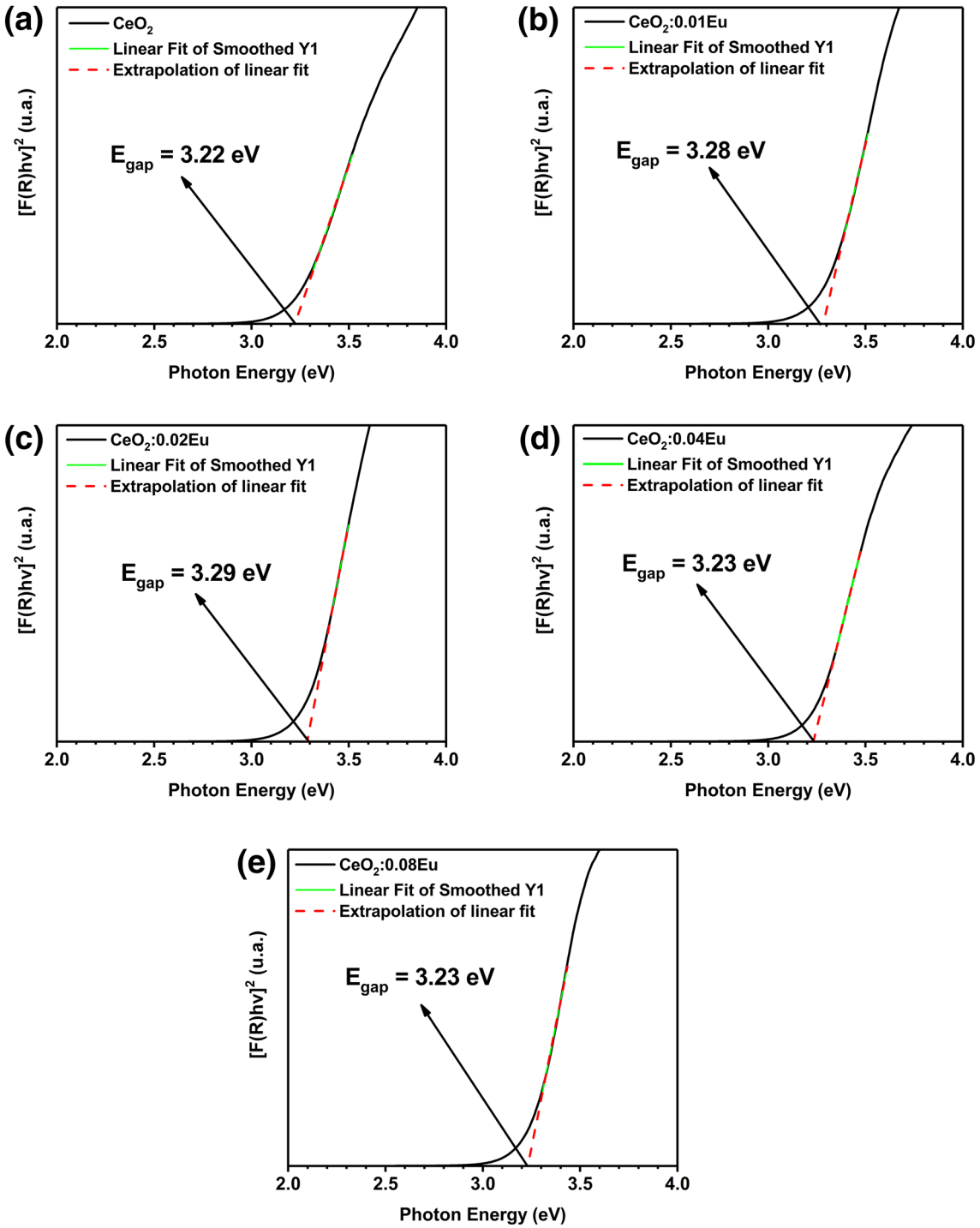

Fig. 7 UV–Vis absorbance spectra of **a** CeO_2, **b** CeO_2:0.01Eu^{3+}, **c** CeO_2:0.02Eu^{3+}, **d** CeO_2:0.04Eu^{3+} and **e** CeO_2:0.08Eu^{3+}

3.5 Photocatalytic activity

The photocatalytic activity of the CeO_2:Eu^{3+} samples was measured with Rhodamine B dye (RhB) under UV–Vis radiation for 200 min (Fig. 8). Through the variation of the concentration of RhB, it is perceived that the increase of Eu^{3+} concentration favors the photocatalytic activity. This fact can be attributed to the introduction of intermediate levels of the dopant in the conduction band of CeO_2 [78]. The Eu^{3+} receives electrons from the conduction band of CeO_2, transforming itself into Eu^{2+} and carrying e^- to react with dissolved O_2, forming superoxide radicals, causing the ions

Table 2 Comparative results between the E_{gap} values of CeO_2:xEu^{3+} (x = 0, 0.01, 0.02, 0.04 and 0.08 mol%) obtained in this work and those reported in the literature

Sample	E_{gap} (eV)	Synthesis method	References
CeO_2	3.22	USP	This work
CeO_2:0.01Eu^{3+}	3.28	USP	This work
CeO_2:0.02Eu^{3+}	3.29	USP	This work
CeO_2:0.04Eu^{3+}	3.23	USP	This work
CeO_2:0.08Eu^{3+}	3.23	USP	This work
CeO_2:Eu^{3+}	3.23	USP	[53]
CeO_2:0.01Cd^{2+}	3.63	Sol–gel	[14]
CeO_2:0.1Zr^{4+}	3.36	Precipitation	[71]
CeO_2:0.09Cr^{3+}	3.41	Sonochemical	[72]

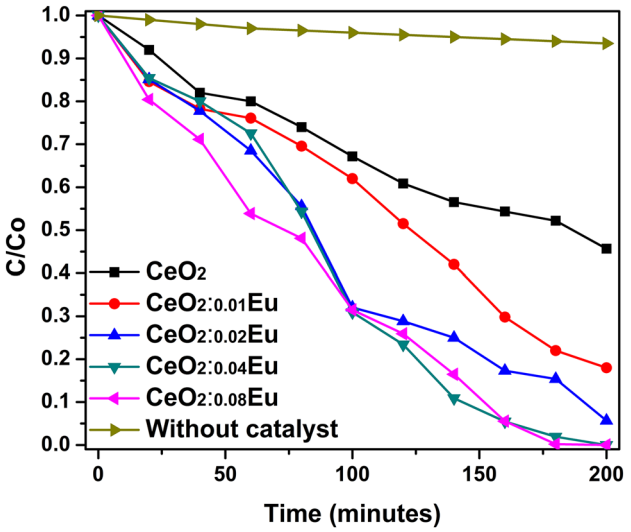

Fig. 8 Variation of the Rhodamine B degradation as a function of the time of CeO_2:xEu^{3+} (x = 0, 0.01, 0.02, 0.04 and 0.08 mol%) under UV–Vis radiation

to act as mediators of surface charge transfer [79–81]. Stefan et al. [82] synthesized Eu^{3+} doped TiO_2 varying from 0 to 12% for the Fe_3O_4 coating and found that by increasing the doping to 10%, it also increased the degradation of RhB, whereas the composition with 12% of Eu^{3+} showed a worse result than the pure compound. As seen in the Raman spectra, the substitution of Ce^{4+} cations by Eu^{3+} cations generate oxygen vacancies, due to the difference in atomic radius and valence, which act in the generation of electron/hole pairs (e^-/h^+), which act directly in the generation of hydroxyl radicals ($OH^{\cdot}$), activating the indirect oxidation mechanism, increasing the photocatalytic efficiency. Mittal et al. [83] showed that the addition of noble metals, such as gold and silver, in the cerium oxide lattice, promotes the generation of oxygen vacancies, which increase the rate of e^-/h^+ pairs generation, increasing the material photocatalytic efficiency.

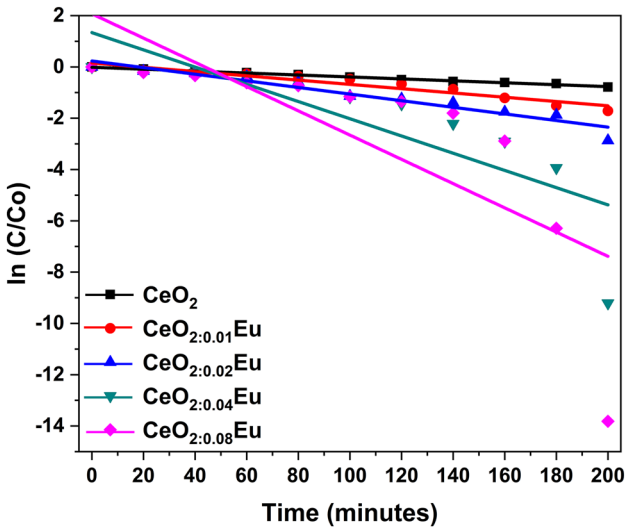

Fig. 9 Evolution of photodegradation of kinetic

Table 3 The apparent first-order rate constant, k of photocatalytic degradation and correlation coefficient, R^2

Sample	$k \times 10^{-3}$ (min^{-1})	R^2
CeO_2	4.02	0.9918
CeO_2:0.01Eu^{3+}	6.46	0.9928
CeO_2:0.02Eu^{3+}	9.53	0.8538
CeO_2:0.04Eu^{3+}	11.79	0.8329
CeO_2:0.08Eu^{3+}	14.17	0.6760

Moreover, as seen through the images obtained by FESEM, the increase in Eu^{3+} concentration distorts the spherical morphology of CeO_2 particles, possibly increasing their surface area, favoring the photocatalytic activity [84]. Chen et al. [85] showed that the increase on the surface area favors the photocatalytic activity of CeO_2 versus methylene blue.

The photocatalytic process can be described by a kinetic model of the first order, regarding the RhB absorbance [86]

$$\frac{-\ln Ct}{Co} = ki \times t \quad (1)$$

where Ct is the RhB absorbance at time t, Co is the initial absorbance; t is the irradiation time and ki is the kinetic constant.

The results obtained are shown in Fig. 9. The graph shows the linear relationship with the irradiation time. The kinetic constant and the correlation coefficient are shown in Table 3. With the obtained data, we can see that the correlation coefficient R^2 decreases as Eu^{3+} increases, indicating the non-linear behavior of the dye degradation. While the

kinetic constant K increases, showing that the increase of Eu^{3+} concentration favors the RhB degradation.

For more information about CeO_2 photocatalytic mechanism, inhibitors of h^+,.OH and e^- were used. Figure 10 shows the C/C_0 curves of the Rhodamine B for the samples of pure CeO_2 and doped with 8% Eu^{3+}. According to Fig. 10, the addition of EDTA and isopropyl alcohol reduces the photocatalytic activity, whereas the use of silver nitrate increases the discoloration of Rhodamine B. These results indicate that the main mechanism acting on the photocatalytic activity consists of the O_2^-, where using EDTA for the h^+ suppression increases the amount of electrons in the CeO_2 conduction band [87]. The second mechanism act in the dye oxidation, where using isopropyl alcohol the suppression of the $^{\cdot}OH$ radicals occurs, reducing its oxidative capacity [88]. The use of $AgNO_3$ accelerated degradation of Rhodamine B, indicating that electron suppression acts to increase the amount of charge (h^+) on the surface of the CeO_2 particles available to react with the water molecules available in the medium, increasing the amount of hydroxyl radicals generated during the catalytic process [58, 89]. Thus, it is observed that the defects generated in the CeO_2 lattice by the doping with europium increase the performance of all mechanisms present in the photocatalytic process.

The ultrasonic spray pyrolysis method is characteristic of the production of materials with spherical morphology, where the alteration of synthesis parameters such as reaction time, starting materials and flow velocity influence the densification and surface morphology of the spheres [90, 91]. The surface area is an important factor for the photocatalytic activity, where particles with larger surface areas usually present better results [92]. Obtaining hollow spheres provides a larger surface area available for photocatalytic performance, counterbalancing the negative effect of the large diameters of the spheres. Deepthi et al. [93] obtained CeO_2 doped with Eu^{3+} by hydrothermal method, with a time of synthesis ranging from 4 to 12 h, where they degraded 95% of MB dye after 180 min. On the other hand, Singh et al. [94] obtained La doped CeO_2 by co-precipitation method, calcining at 850 °C for 2 h, reducing 99.9% of the MB dye concentration after 180 min for the 1% a sample. In our work, CeO_2:xEu was obtained quickly, easily and continuously, and degraded 100% RhB after 200 min. Thus, the ultrasonic spray pyrolysis technique, as a continuous and simple method, becomes attractive in obtaining materials for a wide range of applications.

4 Conclusions

Particles with pure phase of CeO_2:xEu^{3+} (x = 0, 0.01, 0.02, 0.04 and 0.08 mol%) are efficiently obtained by the ultrasonic spray pyrolysis method. This method allows us to obtain the desired phase quickly and without the need for subsequent calcination. The Raman spectra illustrate the appearance of bands at 534 and 600 cm^{-1}, reinforcing that doping occurred ideally, with cationic substitution occurring, where the Eu^{3+} atoms replace the Ce^{4+} atoms in the CeO_2 lattice. The images obtained by FESEM show that the increase of the concentration of Eu^{3+} in the CeO_2 lattice promotes an increase on the surface irregularities of the microspheres. The addition of Eu^{3+} promotes the generation of intermediate levels in the conduction band of CeO_2, which formed superoxides, considerably increasing the photocatalytic power of the material, being a promising photocatalytic material for RhB dye degradation. The scavengers analysis

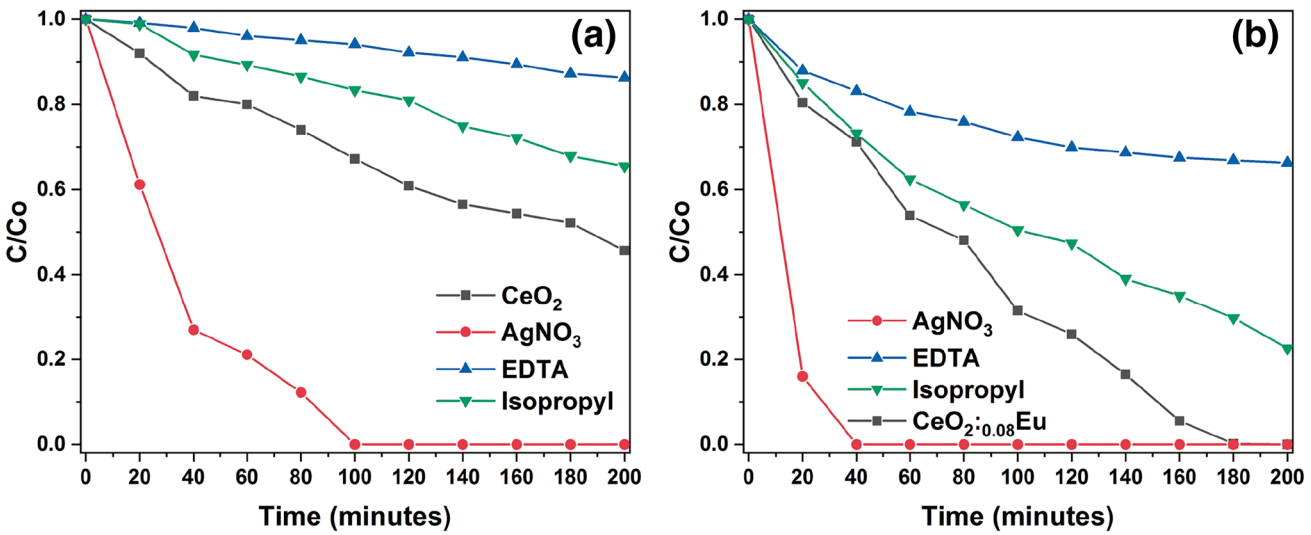

Fig. 10 Variation of the Rhodamine B dye concentration for the **a** CeO_2 and **b** CeO_2:0.08 Eu^{3+} samples with and without charge inhibitors

indicated that the doping with europium enhanced the effects of the charge (e^- and h^+) and reactive species ($^{\cdot}OH$ and O_2^{-}).

Acknowledgment The authors thank the following Brazilian research financing institutions for financial support: A.A.G. Santiago acknowledge financial support from National Council for Scientific and Technological Development—CNPq. Sao Paulo Research Foundation—FAPESP (Processo 2013/07296-2), (2016/23891-6). Coordination for the Improvement of Higher Education Personnel (CAPES)—Brazil (CAPES)—Finance Code 001 and CAPES/PROCAD 2013/2998/2014 and Graduate Program in Materials Science and Engineering (PPGCEM-UFRN).

References

1. N. Reddy, L. Chen, Y. Zhang, Y. Yang, J. Clean. Prod. **65**, 561–567 (2014)
2. J. Dasgupta, J. Sikder, S. Chakraborty, S. Curcio, E. Drioli, J. Environ. Manage. **147**, 55–72 (2015)
3. F. Deniz, R.A. Kepekci, Fibers Polym. **18**, 278–284 (2017)
4. E. Sahinkaya, A. Yurtsever, Ö. Çınar, Sep. Purif. Technol. **174**, 445–454 (2017)
5. K. Intarasuwan, P. Amornpitoksuk, S. Suwanboon, P. Graidist, Sep. Purif. Technol. **177**, 304–312 (2017)
6. Y. Yuan, P. Shen, Q. Li et al., J. Alloys Compd. **700**, 12–17 (2017)
7. C. Lv, J. Sun, G. Chen et al., Appl. Catal. B **208**, 14–21 (2017)
8. G. Han, W. Wang, B. Liu et al., Appl. Catal. B **208**, 94–103 (2017)
9. X. Zhang, A. Tang, Y. Jia, Y. Wang, H. Wang, S. Zhang, J. Alloys Compd. **701**, 16–22 (2017)
10. T. Zhang, M. Liu, Y. Meng, B. Huang, X. Pu, X. Shao, Sep. Purif. Technol. **206**, 149–157 (2018)
11. Y. Soltanabadi, M. Jourshabani, Z. Shariatinia, Sep. Purif. Technol. **202**, 227–241 (2018)
12. M.M. Ibrahim, S.A. El-Molla, S.A. Ismail, J. Mol. Struct. **1158**, 234–244 (2018)
13. A. Khataee, P. Gholami, D. Kalderis, E. Pachatouridou, M. Konsolakis, Ultrason. Sonochem. **41**, 503–513 (2018)
14. S. Gnanam, V. Rajendran, J. Alloys Compd. **735**, 1854–1862 (2018)
15. K. Mani Rahulan, N. Angeline Little Flower, R. Annie Sujatha, P. Mohana Priya, C. Gopalakrishnan, Optics Laser Technol. **101**, 358–362 (2018)
16. V. Shanmugam, R. Zapf, V. Hessel, H. Pennemann, G. Kolb, Appl. Catal. B **226**, 403–411 (2018)
17. C. Liu, H. Tai, P. Zhang et al., Sens. Actuators B **261**, 587–597 (2018)
18. X. Ma, P. Lu, P. Wu, Ceram. Int. **44**, 5284–5290 (2018)
19. M. Yin, W. Qiu, L. Song et al., ChemistrySelect **3**, 2683–2691 (2018)
20. Z. Xiaolong, D. Dong, L. Guijing, F. Wenjie, Y. Sen, S. Zhanbo, Nanotechnology **29**, 095606 (2018)
21. Q. Sun, Z. Fu, Z. Yang, Ceram. Int. **44**, 3707–3711 (2018)
22. Y. Xu, N. Farandos, M. Rosa et al., Int. J. Appl. Ceram. Technol. **15**, 315–327 (2018)
23. K.M. Kumar, M. Mahendhiran, M.C. Diaz et al., Mater. Lett. **214**, 15–19 (2018)
24. W.M. Al-Shawafi, N. Salah, A. Alshahrie et al., J. Mater. Sci.: Mater. Med. **28**, 177 (2017)
25. L. Shen, H. Zhang, G. Liu, H. Fang, J. Mater. Sci.: Mater. Electron. **29**, 2045–2050 (2018)
26. D. Chandrakar, J.K. Saluja, N.S. Suryanarayana et al., J. Mater. Sci.: Mater. Electron. **28**, 17271–17277 (2017)
27. D. Chandrakar, J. Kaur, V. Dubey, N.S. Suryanarayana, Y. Parganiha, Luminescence **30**, 1201–1206 (2015)
28. L. Shao-You, Z. Cheng-Gang, Z. Shi-Biao, Z. Wei-Guo, F. Qing-Ge, Sci. Adv. Mater. **10**, 155–164 (2018)
29. C. Tang, B. Sun, J. Sun et al., Catal. Today **281**, 575–582 (2017)
30. A. Gogoi, K.C. Sarma, Mater. Chem. Phys. **194**, 327–336 (2017)
31. E.A. Derevyannikova, T.Y. Kardash, L.S. Kibis et al., Phys. Chem. Chem. Phys. **19**, 31883–31897 (2017)
32. H. Zheng, Y. Hong, J. Xu, B. Xue, Y.-X. Li, Catal. Commun. **106**, 6–10 (2018)
33. A. Phuruangrat, S. Thongtem, T. Thongtem, Mater. Lett. **196**, 61–63 (2017)
34. A. Phuruangrat, T. Thongtem, S. Thongtem, Mater. Lett. **193**, 161–164 (2017)
35. A.A. Farghali, M.H. Khedr, S.I. El-Dek, A.E. Megahed, Ultrason. Sonochem. **42**, 556–566 (2018)
36. B. Bayyappagari, K. Shaik, M.R. Nasina, O. Inturu, S.R. Dugasani, Optik—Int. J. Light Electron Opt. **154**, 821–827 (2018)
37. P.N. Medeiros, A.A.G. Santiago, E.A.C. Ferreira et al., J. Alloys Compd. **747**, 1078–1087 (2018)
38. M. Kundu, G. Karunakaran, E. Kolesnikov et al., J. Ind. Eng. Chem. **59**, 90–98 (2018)
39. A. Masud, Y. Cui, J.D. Atkinson, N. Aich, J. Nanopart. Res. **20**, 64 (2018)
40. Q. Bkour, K. Im, O.G. Marin-Flores, M.G. Norton, S. Ha, J. Kim, Appl. Catal. A **553**, 74–81 (2018)
41. N. Shatrova, A. Yudin, V. Levina et al., Mater. Res. Bull. **99**, 189–195 (2018)
42. Y. Li, X. Li, Z. Wang, H. Guo, J. Wang, J. Energy Chem. **27**, 447–450 (2018)
43. H. Das, N. Debnath, A. Toda et al., Adv. Powder Technol. **29**, 283–288 (2018)
44. A.A.G. Santiago, L.X. Lovisa, P.N. Medeiros et al., Ultrason. Sonochem. **56**, 14–24 (2019)
45. P. Majerič, D. Jenko, B. Friedrich, R. Rudolf, Adv. Powder Technol. **28**, 876–883 (2017)
46. Z. Cheng, P. Foroughi, A. Behrens, Ceram. Int. **43**, 3431–3434 (2017)
47. H. Shimada, T. Yamaguchi, T. Suzuki, H. Sumi, Y. Fujishiro, Adv. Powder Technol. **27**, 1438–1445 (2016)
48. H.J. Park, G.B. Kim, S.J. Jung et al., J. Ceramic Process. Res. **17**, 818–824 (2016)
49. B. Li, X. Shao, Y. Hao, Y. Zhao, RSC Adv. **5**, 85640–85645 (2015)
50. S.-J. Shih, W.-L. Tzeng, W.-L. Kuo, Surf. Coat. Technol. **259**, 302–309 (2014)
51. C. Goulart, E. Djurado, J. Eur. Ceram. Soc. **33**, 769–778 (2013)
52. S.-J. Shih, Y.-Y. Wu, C.-Y. Chen, C.-Y. Yu, J. Nanopart. Res. **14**, 879 (2012)
53. K.Y. Jung, J.C. Lee, D.S. Kim, B.-K. Choi, W.-J. Kang, J. Lumin. **192**, 1313–1321 (2017)
54. B.H. Min, J.C. Lee, K.Y. Jung, D.S. Kim, B.-K. Choi, W.-J. Kang, RSC Adv. **6**, 81203–81210 (2016)
55. C.R.R. Almeida, L.X. Lovisa, A.A.G. Santiago et al., J. Mater. Sci.: Mater. Electron. **28**, 16867–16879 (2017)
56. A.A.G. Santiago, C.R.R. Almeida, R.L. Tranquilin et al., Ceram. Int. **44**, 3775–3786 (2018)
57. C.-Y. Huang, R.-T. Guo, W.-G. Pan et al., J. CO2 Util. **26**, 487–495 (2018)
58. Y.-Y. Li, X. Dong, H.-Q. Zhang, Procedia Eng. **52**, 202–207 (2013)
59. H. Rietveld, J. Appl. Crystallogr. **2**, 65–71 (1969)
60. B. Toby, J. Appl. Crystallogr. **34**, 210–213 (2001)
61. R. Shannon, Acta Crystallogr. A **32**, 751–767 (1976)

62. M.R. Moura, A.P. Ayala, I. Guedes, M. Grimsditch, C.K. Loong, L.A. Boatner, J. Appl. Phys. **95**, 1148–1151 (2004)
63. W.Y. Hernández, O.H. Laguna, M.A. Centeno, J.A. Odriozola, J. Solid State Chem. **184**, 3014–3020 (2011)
64. C. Schilling, A. Hofmann, C. Hess, M.V. Ganduglia-Pirovano, J. Phys. Chem. C **121**, 20834–20849 (2017)
65. B.M. Reddy, T. Vinodkumar, D. Naga Durgasri, A. Rangaswamy, Proc. Natl. Acad. Sci. India A **87**, 155–161 (2017)
66. A. Kremenovic, D.K. Bozanic, A.M. Welsch et al., J. Nanosci. Nanotechnol. **12**, 8893–8899 (2012)
67. V.I. Parvulescu, C. Tiseanu, Catal. Today **253**, 33–39 (2015)
68. G.L. Messing, S.-C. Zhang, G.V. Jayanthi, J. Am. Ceram. Soc. **76**, 2707–2726 (1993)
69. D.R. Lide, *Handbook of Chemistry and Physics*, 85th edn. (CRC Press, Boca Raton, 2004)
70. D.L. Wood, J. Tauc, Phys. Rev. B **5**, 3144–3151 (1972)
71. R. Bakkiyaraj, M. Balakrishnan, G. Bharath, N. Ponpandian, J. Alloys Compd. **724**, 555–564 (2017)
72. B.S. Rohini, H. Nagabhushana, G.P. Darshan et al., J. Alloys Compd. **724**, 897–909 (2017)
73. H. Li, F. Meng, J. Gong, Z. Fan, R. Qin, J. Alloys Compd. **722**, 489–498 (2017)
74. C. Ma, J. Fu, J. Chen et al., Ind. Eng. Chem. Res. **56**, 9090–9097 (2017)
75. J. Wang, Z. Cao, J. Zhang et al., J. Mater. Sci.: Mater. Electron. **28**, 12858–12865 (2017)
76. W. Zou, B. Deng, X. Hu et al., Appl. Catal. B **238**, 111–118 (2018)
77. Y. Ding, J. Wang, S. Xu, K.-Y.A. Lin, S. Tong, Sep. Purif. Technol. **207**, 92–98 (2018)
78. Y. Lu, Y. Lin, T. Xie, S. Shi, H. Fan, D. Wang, Nanoscale **4**, 6393–6400 (2012)
79. J. Tang, X. Chen, Y. Liu et al., J. Phys. Chem. Solids **73**, 198–203 (2012)
80. Q. Yin, R. Qiao, Z. Li, X.L. Zhang, L. Zhu, J. Alloys Compd. **618**, 318–325 (2015)
81. A.S. Weber, A.M. Grady, R.T. Koodali, Catal. Sci. Technol. **2**, 683–693 (2012)
82. M. Stefan, C. Leostean, O. Pana et al., Appl. Surf. Sci. **390**, 248–259 (2016)
83. M. Mittal, A. Gupta, O.P. Pandey, Sol. Energy **165**, 206–216 (2018)
84. F. Dong, T. Xiong, Y. Sun et al., Appl. Catal. B **219**, 450–458 (2017)
85. F. Chen, Y. Cao, D. Jia, Appl. Surf. Sci. **257**, 9226–9231 (2011)
86. M.M. Momeni, M. Hakimian, A. Kazempour, Ceram. Int. **41**, 13692–13701 (2015)
87. S. Xing, T. Li, Y. Gao, J. Liu, Optik **183**, 266–272 (2019)
88. N.A. Portela, S.R.C. Silva, L.F.R. de Jesus et al., Fuel **216**, 681–685 (2018)
89. J. Hao, Y. Jiang, X. Gao, F. Xie, Z. Shao, B. Yi, J. Membr. Sci. **522**, 23–30 (2017)
90. X. Zhao, W. Li, F. Kong et al., Mater. Chem. Phys. **219**, 461–467 (2018)
91. Y. Hwangbo, Y.-I. Lee, J. Alloys Compd. **771**, 821–826 (2019)
92. Z. Lv, Q. Zhong, M. Ou, Appl. Surf. Sci. **376**, 91–96 (2016)
93. N.H. Deepthi, G.P. Darshan, R.B. Basavaraj, B.D. Prasad, H. Nagabhushana, Sens. Actuators B **255**, 3127–3147 (2018)
94. K. Singh, K. Kumar, S. Srivastava, A. Chowdhury, Ceram. Int. **43**, 17041–17047 (2017)